

OPEN ACCESS

Degradation Diagnostics for Commercial Lithium-Ion Cells Tested at -10°C

To cite this article: Christoph R. Birkl *et al* 2017 *J. Electrochem. Soc.* **164** A2644

View the [article online](#) for updates and enhancements.

You may also like

- [A New Battery SOC/SOH/eSOH Estimation Method Using a PBM and Interconnected SPKFs: Part II. SOH and eSOH Estimation](#)
Iker Lopetegi, Gregory L. Plett, M. Scott Trimble et al.

- [Motivation, benefits, and challenges for new photovoltaic material & module developments](#)
G Oreski, J S Stein, G C Eder et al.

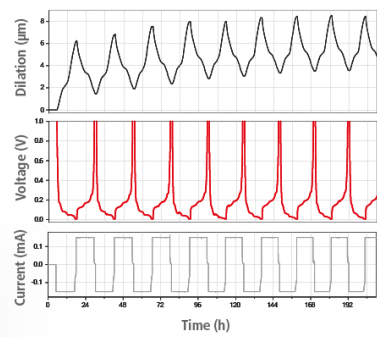
- [Durability and Reliability of EV Batteries under Electric Utility Grid Operations: Path Dependence of Battery Degradation](#)
Matthieu Dubarry, George Baure and Arnaud Devie

Watch Your Electrodes Breathe!

EL-CELL®
electrochemical test equipment

Measure the Electrode Expansion in the Nanometer Range with the ECD-4-nano.

- ✓ Battery Test Cell for Dilatometric Analysis (Expansion of Electrodes)
- ✓ Capacitive Displacement Sensor (Range 250 μm , Resolution $\leq 5 \text{ nm}$)
- ✓ Detect Thickness Changes of the Individual Half Cell or the Full Cell
- ✓ Additional Gas Pressure (0 to 3 bar) and Temperature Sensor (-20 to 80° C)



See Sample Test Results:



Download the Data Sheet (PDF):



Or contact us directly:

📞 +49 40 79012-734

✉️ sales@el-cell.com

🌐 www.el-cell.com



Degradation Diagnostics for Commercial Lithium-Ion Cells Tested at -10°C

Christoph R. Birkl,^{a,*} Euan McTurk,^b Stefanie Zekoll,^{c,*} Felix H. Richter,^c Matthew R. Roberts,^c Peter G. Bruce,^{c,**} and David A. Howey^{a,***,z}

^aDepartment of Engineering Science, University of Oxford, Oxford OX1 3PJ, United Kingdom

^bWMG, University of Warwick, Coventry CV4 7AL, United Kingdom

^cDepartment of Materials, University of Oxford, Oxford OX1 3PH, United Kingdom

Degradation of lithium ion (Li-ion) cells affects both performance and safety of Li-ion batteries. In order to avoid potential safety hazards, it is crucial to detect the onset and extent of critical degradation modes in commercial Li-ion cells. This work demonstrates the application of a diagnostic algorithm to identify and quantify degradation modes of commercial Li-ion pouch cells cycled at -10°C and a C-rate of 2 C. Rapid loss of active negative electrode material was successfully identified and results were validated using 3-electrode cells, scanning electron microscopy (SEM) and energy-dispersive X-ray spectroscopy (EDX). The positive electrode material was less strongly affected by the tests, as found by the diagnostic algorithm and confirmed with EDX and SEM results.

© The Author(s) 2017. Published by ECS. This is an open access article distributed under the terms of the Creative Commons Attribution Non-Commercial No Derivatives 4.0 License (CC BY-NC-ND, <http://creativecommons.org/licenses/by-nc-nd/4.0/>), which permits non-commercial reuse, distribution, and reproduction in any medium, provided the original work is not changed in any way and is properly cited. For permission for commercial reuse, please email: oa@electrochem.org. [DOI: [10.1149/2.1401712jes](https://doi.org/10.1149/2.1401712jes)]

All rights reserved.



Manuscript submitted May 9, 2017; revised manuscript received July 31, 2017. Published September 1, 2017.

Lithium ion (Li-ion) cells degrade as a result of usage and environmental influences, typically resulting in capacity fade and increased internal resistance.^{1–3} Some degradation mechanisms can lead to safety hazards through increased risk of fire or explosion. The deposition of metallic lithium and dendrite formation on graphite negative electrodes (NE) are particularly dangerous mechanisms, since metallic dendrites can pierce the separator and lead to internal short-circuits resulting in thermal runaway.^{4–6} Understanding and detecting lithium plating and dendrite formation are important milestones on the pathway to safer, more reliable Li-ion batteries. Low operating temperatures during charge increase the risk of lithium plating and dendrite formation.^{7–16} This makes it important to assess and model the behavior of Li-ion batteries at low temperatures, which is undertaken in this study.

Arora et al.⁴ proposed a mathematical model to predict lithium deposition on the NE during charge and overcharge, which can be used to determine operational and design limitations in order to minimize safety hazards. Other authors have focused on in-situ detection of lithium plating using electrochemical calorimetry,¹⁷ a combination of an electrochemical model with a particle filter,¹⁸ differential analysis of cell voltage measurements,⁷ measurements of changes in cell thickness in pouch cells,^{19,20} analysis of measured voltage transients and subsequent relaxation,²¹ high precision coulometry²² and impedance spectroscopy.²³

Although in-situ detection of lithium plating is an important advance, safety hazards can be further reduced by detecting the factors leading up to lithium plating before the onset of the plating mechanism itself. Deposition of metallic lithium on graphite NEs occurs under high charging rates, at low charging temperatures and in poorly balanced cells with an excess of active positive electrode (PE) material.^{4,12,24,25} These circumstances are easily avoided in new cells by appropriate cell design and observation of operational limitations such as minimal charging temperature and maximal cell voltages and current rates. However, as cells degrade, active electrode material can be lost, changing the ratio of negative to positive electrode material and the current rates and voltage limits imposed on the remaining active material. Loss of NE material leads to higher current rates on the NE and a higher ratio of active PE to NE material, both of which increase the risk of lithium deposition and associated safety hazards. It is therefore crucial to detect and track the loss of active NE material in order to ensure safe operation of Li-ion batteries throughout their

cycle life. Anseán et al.¹⁶ have made significant progress in this area by applying incremental capacity analysis in order to identify and track lithium plating ex situ under a dynamic drive cycle schedule.

In this work we build on the same concept of degradation modes – loss of lithium inventory (LLI), loss of active PE material (LAM_{PE}) and loss of active NE material (LAM_{NE}) – by applying a diagnostic algorithm, presented in Ref. 26, to identify and quantify the different degradation modes. The degradation modes are estimated by fitting the open circuit voltage (OCV) of Li-ion cells measured at various stages throughout the cells' cycle life. The OCV of the cell is computed from its constituent electrode voltages using the OCV model introduced in Ref. 27.

In this work the diagnostic algorithm was used on commercial Kokam pouch cells (740 mAh) and 3-electrode cells, cycled at -10°C and 2 C, in order to identify and quantify the onset and extent of LAM_{NE} , LAM_{PE} and LLI from OCV measurements. Results were validated by comparing the modeled electrode voltages with the electrode voltages measured on the 3-electrode cells. Further validation was achieved by post-mortem analysis using scanning electron microscopy (SEM) and energy-dispersive X-ray spectroscopy (EDX).

Experimental

Three types of experiments were carried out for this work:

- Electrical tests on half-cells to parameterize the OCV model.
- Electrical tests on 3-electrode cells and unmodified pouch cells to validate the diagnostic algorithm.
- Post-mortem analysis for further validation of the diagnostic algorithm, consisting of SEM and EDX.

Kokam pouch cells, model SLPB 533459H, 740 mAh nominal capacity, were used for all experiments in this work. Half-cells were manufactured from electrode material harvested from the pouch cells. The method for the manufacture of half-cells is described elsewhere.²⁷ The PE material of the Kokam pouch cells is a blend of lithium cobalt oxide (LCO) and lithium nickel cobalt oxide (NCO) and the NE material is graphite. Two half-cells were made—one PE and one NE half-cell.

3-electrode cells were made by inserting a reference electrode, consisting of a copper wire plated with lithium, into the Kokam pouch cells. A detailed account of the method is provided in Ref. 28. In order to ensure that the modification technique used to insert the reference

*Electrochemical Society Student Member.

**Electrochemical Society Member.

^zE-mail: david.howey@eng.ox.ac.uk

Table I. Overview of test subjects. Standard numerals denote cells with reference electrodes and Roman numerals cells without reference electrodes.

Cell ID	Ref electrode	Cycles	CV period	Charact. intervals	Post-mortem
Cell 0	×	0	-	-	SEM, EDX
Cell 1	✓	120	20 min	variable	EDX
Cell 2	✓	70	25 min	10 cycles	-
Cell 3	✓	80	25 min	20 cycles	SEM, EDX
Cell 4	✓	80	25 min	20 cycles	SEM, EDX
Cell I	×	120	20 min	variable	EDX
Cell II	×	80	25 min	20 cycles	SEM, EDX
Cell III	×	80	25 min	20 cycles	-
Cell IV	×	80	25 min	20 cycles	-

Table II. Test procedure cell 1 and I.

Test	Step	Current	Stop-criterion
Charact. (at T = 25°C)	Rest	0 mA	t > 3 h
	CC charge	740 mA	V _{cell} > 4.2 V
	CV charge	variable	I < 40 mA
Cycling (at T = -10°C)	Rest	0 mA	t > 3 h
	C/25 discharge	29.6 mA	V _{cell} < 2.7 V
	Rest	0 mA	t > 3 h
	CC charge	1480 mA	V _{cell} > 4.2 V
	CV charge	variable	t > 20 min
	CC discharge	1480 mA	V _{cell} < 2.7 V

electrodes did not affect the performance and degradation of the cells, unmodified cells were tested alongside the 3-electrode cells.

Electrical cell tests.—A total of nine Kokam 740 mAh pouch cells were used for the experiments. This includes one pristine cell, which did not undergo any electrical tests but was used for comparative post-mortem analysis with SEM and EDX. Reference electrodes were introduced into four of the cells while the remaining four were unmodified. In this paper, the cells containing reference electrodes are labeled with standard numerals and the unmodified cells are labeled with Roman numerals. All cells were subjected to high-rate, low-temperature cycling (constant current (CC) charging followed by constant voltage (CV) charging and CC discharging) at -10°C (which is outside the manufacturer's recommended temperature limits) and repeated low-rate characterization at 25°C. The number of cycles between characterizations and the CV charging period during low-temperature cycling were varied between the different cells. The cell and electrode voltages recorded during the characterization steps were used to parameterize the diagnostic algorithm. Due to the low C-rate used during the characterization steps, the measurements are referred to as pseudo-OCV. Table I gives an overview of the test subjects and the corresponding test conditions. As specified in Table I, SEM and EDX were carried out on a selection of the cells. The cell test procedures are described in Table II for cell 1 and I and in Table III for

all other cells. All experiments were carried out in a Vötsch thermal chamber, using Bio-Logic SP-150 and HCP 1005 battery testers.

Half-cell tests.—The two half-cells—one PE and one NE half-cell—were cycled at a rate of C/25; the same rate as used for the characterization steps of the pouch cells. Given a measured active electrode surface area of 600 cm² and a nominal capacity of 740 mAh, the nominal current density of the pouch cells was 1.233 mAh/cm². Assuming the same nominal current density for the coin cells with a diameter of 12 mm (surface area of 1.767 cm²), a C-rate of C/25 for the coin cells is equivalent to 0.056 mA. The half-cell tests were conducted inside a Vötsch thermal chamber at 25°C using a Bio-Logic SP150 potentiostat. Voltage measurements were recorded every 1 min or 1 mV change. The second cycle was used for the parameterization of the OCV model.

SEM and EDX.—Samples for SEM images and EDX spectra were extracted from the positive and NEs of the pristine cell 0 and cycled pouch cells 1, 4, I and II. The cells were opened in an argon-filled glove box using a ceramic scalpel. Positive and negative electrode sheets were extracted from the cell stack, rinsed with dimethyl carbonate and dried under vacuum for 20 min. Square sections of 5 × 5 mm were cut from both the PE and NE using a scalpel.

Both SEM images and EDX spectra were recorded on a Merlin-60-62 instrument. The SEM images were recorded using a secondary electron detector at a working distance of 8.9–9.2 mm and an accelerating voltage of 2 kV. EDX spectra were recorded at a working distance of 8.2–8.8 mm and an accelerating voltage of 10 kV.

Methodology

The diagnostic algorithm introduced in Ref. 26 is used in this work to identify and quantify the degradation modes in Kokam pouch cells exposed to extreme cycling conditions. The OCV model, presented in, Ref. 27, was parameterized at the beginning of the cell tests by fitting pseudo-OCV measurements of the half-cells and the full-cells. As the cells degrade, more pseudo-OCV measurements were recorded at set intervals. These pseudo-OCV measurements were fitted using the diagnostic algorithm, which computes the degradation modes LLI, LAM_{PE} and LAM_{NE}. The degradation modes were calculated from changes in the pseudo-OCV of the PE and NE, as computed by the diagnostic algorithm. The reference electrodes inserted into the 3-electrode cells allow us to validate the accuracy of the modeled electrode voltages which, by extension, is a measure of the accuracy of the estimated degradation modes. Further validation of the estimated degradation modes was achieved through post mortem analysis of the PE and NE materials by means of SEM imaging and EDX analysis.

OCV model parameter estimation.—This section provides a brief overview of the OCV model and parameter estimation. For a more detailed account, the reader is referred to Ref. 27. The OCV of the electrodes can be described implicitly by

$$x(E^{\text{OC}}) = \sum_{i=1}^N \frac{\Delta x_i}{1 + \exp[(E^{\text{OC}} - E_i^0)a_i e/kT]} \quad [1]$$

where x is the fraction of intercalated lithium, ranging from 0 for fully de-intercalated to 1 for fully intercalated electrode material^d, E^{OC} is the OCV of the electrode, Δx_i is the fraction of lithium intercalated in phase i of the electrode material, E_i^0 is the standard redox potential of phase i of the material, a_i is a dimensionless factor for the approximation of effects of interaction energies of intercalated ions on the electrode potential,²⁷ e is the elementary charge, k is the Boltzmann constant and T is the temperature. The particular electrode material used in this work was found to exhibit five observable phase

Table III. Test procedure cells 2, 3, 4, II, III, IV.

Test	Step	Current	Stop-criterion
Charact. (at T = 25°C)	Rest	0 mA	t > 3 h
	CC discharge	370 mA	V _{cell} < 2.7 V
	C/25 charge	29.6 mA	V _{cell} > 4.2 V
Cycling (at T = -10°C)	C/25 discharge	29.6 mA	V _{cell} < 2.7 V
	Rest	0 mA	t > 3 h
	CC charge	1480 mA	V _{cell} > 4.2 V
	CV charge	variable	t > 25 min
	CC discharge	1480 mA	V _{cell} < 2.7 V

^dIn this work we consider the electrode material to be fully de-intercalated ($x = 0$) and fully intercalated ($x = 1$) at the specified maximum and minimum potential limits of the materials.

transitions,²⁶ which corresponds to the number of phases used to define N in Equation 1. Equation 1 can thus be written for the PE and the NE as

$$x_{\text{PE}}(E_{\text{PE}}^{\text{OC}}) = \sum_{i=1}^5 \frac{\Delta x_{\text{PE},i}}{1 + \exp[(E_{\text{PE}}^{\text{OC}} - E_{0,\text{PE},i})a_{\text{PE},i}e/kT]} \quad [2]$$

and

$$x_{\text{NE}}(E_{\text{NE}}^{\text{OC}}) = \sum_{i=1}^5 \frac{\Delta x_{\text{NE},i}}{1 + \exp[(E_{\text{NE}}^{\text{OC}} - E_{0,\text{NE},i})a_{\text{NE},i}e/kT]}. \quad [3]$$

Given the known ranges of the OCV of the electrode materials, x_{NE} and x_{PE} can be calculated numerically using Equations 2 and 3. The parameters Δx_i , E_i^0 and a_i were calculated for each electrode and each phase i by fitting the recorded pseudo-OCV measurements of the half-cells using Matlab's constrained nonlinear optimization function *fmincon*. The parameters can be summarized for the PE by the matrix

$$\theta_{\text{PE}} = \begin{bmatrix} E_{\text{PE},1}^0 & \Delta x_{\text{PE},1} & a_{\text{PE},1} \\ E_{\text{PE},2}^0 & \Delta x_{\text{PE},2} & a_{\text{PE},2} \\ \vdots & \vdots & \vdots \\ E_{\text{PE},5}^0 & \Delta x_{\text{PE},5} & a_{\text{PE},5} \end{bmatrix}, \quad [4]$$

and for the NE by the matrix

$$\theta_{\text{NE}} = \begin{bmatrix} E_{\text{NE},1}^0 & \Delta x_{\text{NE},1} & a_{\text{NE},1} \\ E_{\text{NE},2}^0 & \Delta x_{\text{NE},2} & a_{\text{NE},2} \\ \vdots & \vdots & \vdots \\ E_{\text{NE},5}^0 & \Delta x_{\text{NE},5} & a_{\text{NE},5} \end{bmatrix}. \quad [5]$$

The parameters in θ_{PE} and θ_{NE} were estimated by minimizing the root-mean-squared error (RMSE) between the measured and the computed pseudo-OCVs of the PE and NE half-cells using the objective functions

$$\arg \min_{\theta_{\text{PE}}} \text{RMSE}(\theta_{\text{PE}}) = \sqrt{\frac{\sum_{i=1}^n (\hat{E}_{\text{PE},i}^{\text{OC}}(\theta_{\text{PE}}) - E_{\text{PE},i}^{\text{OC}})^2}{n}} \quad [6]$$

$$\arg \min_{\theta_{\text{NE}}} \text{RMSE}(\theta_{\text{NE}}) = \sqrt{\frac{\sum_{i=1}^n (\hat{E}_{\text{NE},i}^{\text{OC}}(\theta_{\text{NE}}) - E_{\text{NE},i}^{\text{OC}})^2}{n}}, \quad [7]$$

where $\hat{E}_{\text{PE},i}^{\text{OC}}$ and $\hat{E}_{\text{NE},i}^{\text{OC}}$ are the estimated pseudo-OCV of the PE and the NE, respectively and n is the number of data points of the pseudo-OCV measurements.

A full-cell does not utilize the entire available capacity ranges of the electrodes, which means that the PE and the NE are not fully lithiated and de-lithiated during the charge and discharge within a full-cell. The capacity ranges of the electrodes within the full-cell were estimated by fitting the cell's pseudo-OCV. The cell voltage is calculated from the electrode voltages by

$$E_{\text{cell}}^{\text{OC}} = E_{\text{PE}}^{\text{OC}}(x_{\text{PE},\text{cell}}) - E_{\text{NE}}^{\text{OC}}(x_{\text{NE},\text{cell}}), \quad [8]$$

where $x_{\text{PE},\text{cell}}$ and $x_{\text{NE},\text{cell}}$ are the capacity ranges utilized within the full-cell. These capacity ranges are estimated by minimizing the objective function

$$\arg \min_{x_{\text{PE},\text{cell}}, x_{\text{NE},\text{cell}}} \text{RMSE}(x_{\text{PE},\text{cell}}, x_{\text{NE},\text{cell}}) = \sqrt{\frac{\sum_{i=1}^n (\hat{E}_{\text{cell},i}^{\text{OC}}(x_{\text{PE},\text{cell}}, x_{\text{NE},\text{cell}}) - E_{\text{cell},i}^{\text{OC}})^2}{n}} \quad [9]$$

where n is the number of data points recorded for $E_{\text{cell}}^{\text{OC}}$.

In the final step of the parameter estimation procedure, the parameters in θ_{PE} and θ_{NE} are refined by fitting the pseudo-OCV of the electrodes measured on the 3-electrode cells. This step is not strictly

necessary but it was conducted in this work in order to minimize inaccuracies in the initial fit of the pseudo-OCV data, which could affect the estimation of degradation modes at later stages in the cells's life. The objective function used to refine the estimates of parameters in θ_{PE} and θ_{NE} is

$$\begin{aligned} \arg \min_{\theta_{\text{PE}}, \theta_{\text{NE}}} \text{RMSE}(\theta_{\text{PE}}, \theta_{\text{NE}}) = & \sqrt{\frac{\sum_{i=1}^n (\hat{E}_{\text{PE},\text{cell},i}^{\text{OC}}(\theta_{\text{PE}}) - E_{\text{PE},\text{cell},i}^{\text{OC}})^2}{n}} \\ & + \sqrt{\frac{\sum_{i=1}^n (\hat{E}_{\text{NE},\text{cell},i}^{\text{OC}}(\theta_{\text{NE}}) - E_{\text{NE},\text{cell},i}^{\text{OC}})^2}{n}}. \end{aligned} \quad [10]$$

The estimated parameters in θ_{PE} and θ_{NE} are used in Equations 2, 3 and 8 in order to compute the cell voltage. The parameterization of the OCV model was only carried out once at the beginning of the cells' life.

Estimation of degradation modes.—The degradation modes LLI, LAM_{PE} and LAM_{NE} were estimated using a diagnostic algorithm which is described in detail in Ref. 26. This section gives a brief overview of the application of this algorithm. The degradation modes LLI, LAM_{PE} and LAM_{NE} can be derived from the capacity ranges of the PE and the NE used within the full-cell by

$$\text{LLI}_i = 1 - x_{\text{cell},i} - \frac{x_{\text{NE},\text{EoD},0} - x_{\text{NE},\text{EoD},i}}{x_{\text{NE},0}} + \frac{x_{\text{PE},\text{EoC},0} - x_{\text{PE},\text{EoC},i}}{x_{\text{PE},\text{cell},0}} \quad [11]$$

$$\text{LAM}_{\text{PE},i} = \frac{x_{\text{PE},\text{EoD},i} - x_{\text{PE},\text{EoC},0}}{x_{\text{PE},\text{cell},0}} \quad [12]$$

$$\text{LAM}_{\text{NE},i} = \frac{x_{\text{NE},\text{EoC},0} - x_{\text{NE},\text{EoC},i}}{x_{\text{NE},\text{cell},0}}, \quad [13]$$

where

$$x_{\text{cell}} = \{x_{\text{cell},\text{EoC}} \dots x_{\text{cell},\text{EoD}}\} \quad [14]$$

$$x_{\text{PE},\text{cell}} = \{x_{\text{PE},\text{EoC}} \dots x_{\text{PE},\text{EoD}}\} \quad [15]$$

$$x_{\text{NE},\text{cell}} = \{x_{\text{NE},\text{EoC}} \dots x_{\text{NE},\text{EoD}}\}. \quad [16]$$

The subscript EoC indicates end of charge and the subscript EoD end of discharge. Values corresponding to the first characterization cycle are marked with the subscript 0 and values corresponding to characterization cycle i are marked with the subscript i . The degradation modes, summarized by

$$\theta_{\text{deg}} = [\text{LLI}, \text{LAM}_{\text{PE}}, \text{LAM}_{\text{NE}}], \quad [17]$$

were estimated by minimizing the objective function

$$\arg \min_{\theta_{\text{deg}}} \text{RMSE}(\theta_{\text{deg}}) = \sqrt{\frac{\sum_{i=1}^n (\hat{E}_{\text{cell},i}^{\text{OC}}(\theta_{\text{deg}}) - E_{\text{cell},i}^{\text{OC}})^2}{n}}. \quad [18]$$

The estimation of the parameters in θ_{deg} was repeated at every characterization cycle i throughout the cells' lifetime.

Post-mortem analysis.—SEM and EDX analyses were carried out on NE and PE samples of a pristine cell (cell 0), an unmodified cell after 80 cycles (cell II) and a modified, 3-electrode cell after 80 cycles (cell 4). EDX analyses were also conducted after 120 cycles on NE and PE samples of the unmodified cell I, and the modified, 3-electrode cell 1.

SEM analysis of the electrode areas after cell disassembly provides information about their morphology, which can indicate the formation of coatings or large cracks in the active materials of NE and PE.

EDX reveals the elemental composition of the electrodes near the electrode surface. Changes in composition between the samples of the pristine cell and the cycled cells provide insights into the chemical changes near the electrodes' surface, which could be due to surface film formation, metallic depositions or decomposition reactions affecting active materials and/or the electrolyte.

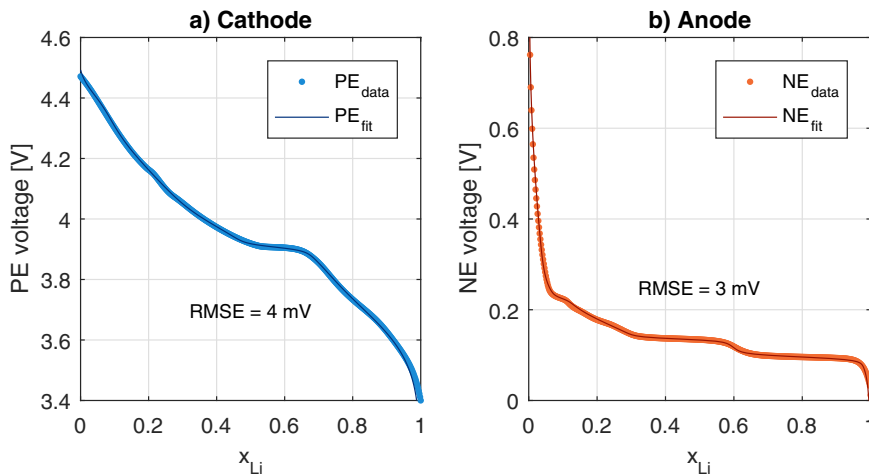


Figure 1. Pseudo-OCV fitting results of a) PE half-cell and b) NE half-cell.

Post-mortem experiments were conducted in order to validate, qualitatively, the degradation modes estimated using the diagnostic algorithm. Moreover, the analyses should reveal whether the cell modification had an effect on cell degradation by comparing the results of modified and unmodified cells.

Results and Discussion

OCV model parameter estimation results.—The results of the initial pseudo-OCV fits of the PE and NE half-cells are displayed in Figure 1. High quality fits were achieved with a RMSE of 4 mV for the PE and 3 mV for the NE. Estimated OCV model parameters of the PE and NE are listed in Table IV. The parameters Δx_i are fractions of the total normalized electrode capacity utilized within the cell and parameters a_i are dimensionless.

The initial estimates of the OCV parameters for the PE and NE were used as initial guesses to fit the pseudo-OCV of the electrodes measured on the 3-electrode cells. The fitting results obtained for cells 1, 2 and 3 are displayed in Figure 2. PE and cell voltages are plotted on the left y-axes and NE voltages on the right y-axis, against depth of discharge. The RMSE of the fits of electrode and cell OCVs are indicated in the figure. RMSE values do not exceed 1.7 mV for the electrode fits and 2.4 mV for the cell fits of all cells.

Electrical cell test results.—Electrical cell tests consisted of low-temperature cycling and frequent low-rate (pseudo-OCV) characterizations. Figure 3 shows the electrode and cell voltages recorded on three 3-electrode cells (cell 1, 2 and 3) during a low-temperature cycle. PE and cell voltages are plotted on the left y-axis and NE voltages on the right y-axis, against time.

Cell 1 was exposed to a shorter CV charging period than cells 2 and 3. From the voltage data in Figure 3 it is evident that the low temperature significantly affects the cells' overpotentials, which is reflected by a rapid increase in PE and cell voltages during charge and a pronounced voltage drop of PE and cell voltages at the beginning of discharge. Moreover, the low temperature and relatively high charging

current rate of 2 C caused the NE voltage to drop below 0 V shortly after the start of the charging step, until the start of the discharging step. At negative potentials, metallic lithium can be plated on the NE surface, creating a safety hazard if dendrites are formed which could pierce the separator and lead to internal short-circuits.

No internal short-circuits were observed during the cell tests but all cells exposed to low-temperature cycling faded rapidly, as illustrated in Figure 4, which shows pseudo-OCV measurements recorded on cells 3, 4, II, III and IV during the first characterization cycle (Figure 4a) and after 80 cycles (Figure 4b). The cells lost around one third of their initial capacity after 80 cycles. The spread in measured capacities among the cells increased from a standard deviation of 3.2 mAh or 0.4% of the mean at cycle 1 to 34.7 mAh or 6.9% of the mean at cycle 80. Notably, there was no significant difference in capacity fade between the modified (3-electrode) cells and the unmodified cells at cycle 80, which is a good indication that the modification did not affect the cells' cycle life.

Estimation of degradation modes.—Based on the OCV model, whose parameters were identified in OCV model parameter estimation results section, the diagnostic algorithm was used to estimate the degradation modes by fitting the cells' pseudo-OCV measurements of all recorded characterization cycles. Only the pseudo-OCV of the full-cells was used in the diagnostic algorithm to estimate the degradation modes. The fitting results obtained for cells 1, 2 and 3 are displayed in Figure 5. The left column of Figure 5 shows the voltage data and fitting results of the cells, PEs and NEs for all recorded characterization cycles. Pseudo-OCV measurements of full-cells, PEs and NEs are illustrated with broken lines and fitted voltages with solid lines. Cell and PE voltages are plotted against DoD on the left axes and NE voltages on the right axes. The right column of Figure 5 shows the corresponding fitting errors of the cells, PEs and NEs, plotted against DoD.

High fitting accuracies were achieved for both the cell and electrode voltages with fitting errors not exceeding 20 mV for a DoD of less than 90% for any characterization cycle. Maximal RMSE values for all fits of the cell, PE and NE voltages of cells 1, 2 and 3 are listed in Table V and do not exceed 16 mV at any characterization cycle. Low residuals and RMSE values for the electrode voltage fits are indicators that the PE and NE voltages of all three cells were accurately modeled by the diagnostic algorithm throughout the tests. There is a general trend of slight increases in residuals with increasing cycle numbers for all cells, which indicates that some minor effects of degradation on the cells' OCVs may not be captured by the three degradation modes LLI, LAM_{PE} and LAM_{NE}.

The degradation modes LLI, LAM_{PE} and LAM_{NE} estimated with the diagnostic algorithm are displayed in Figure 6. Degradation modes are plotted against cycle number for cell 1 (a), cell 2 (b) and cell 3 (c). Measured capacity loss is also displayed. The accuracies of estimated

Table IV. OCV model parameters.

Phase	PE			NE		
	$E_{\text{PE},i}^0$	$\Delta x_{\text{PE},i}$	$a_{\text{PE},i}$	$E_{\text{NE},i}^0$	$\Delta x_{\text{NE},i}$	$a_{\text{NE},i}$
P ₁	4.418 V	0.064	0.803	0.374 V	0.063	0.187
P ₂	4.175 V	0.266	0.298	0.225 V	0.030	8.274
P ₃	3.967 V	0.196	0.597	0.164 V	0.327	0.933
P ₄	3.907 V	0.151	4.674	0.135 V	0.241	11.838
P ₅	3.699 V	0.323	0.295	0.096 V	0.338	8.505

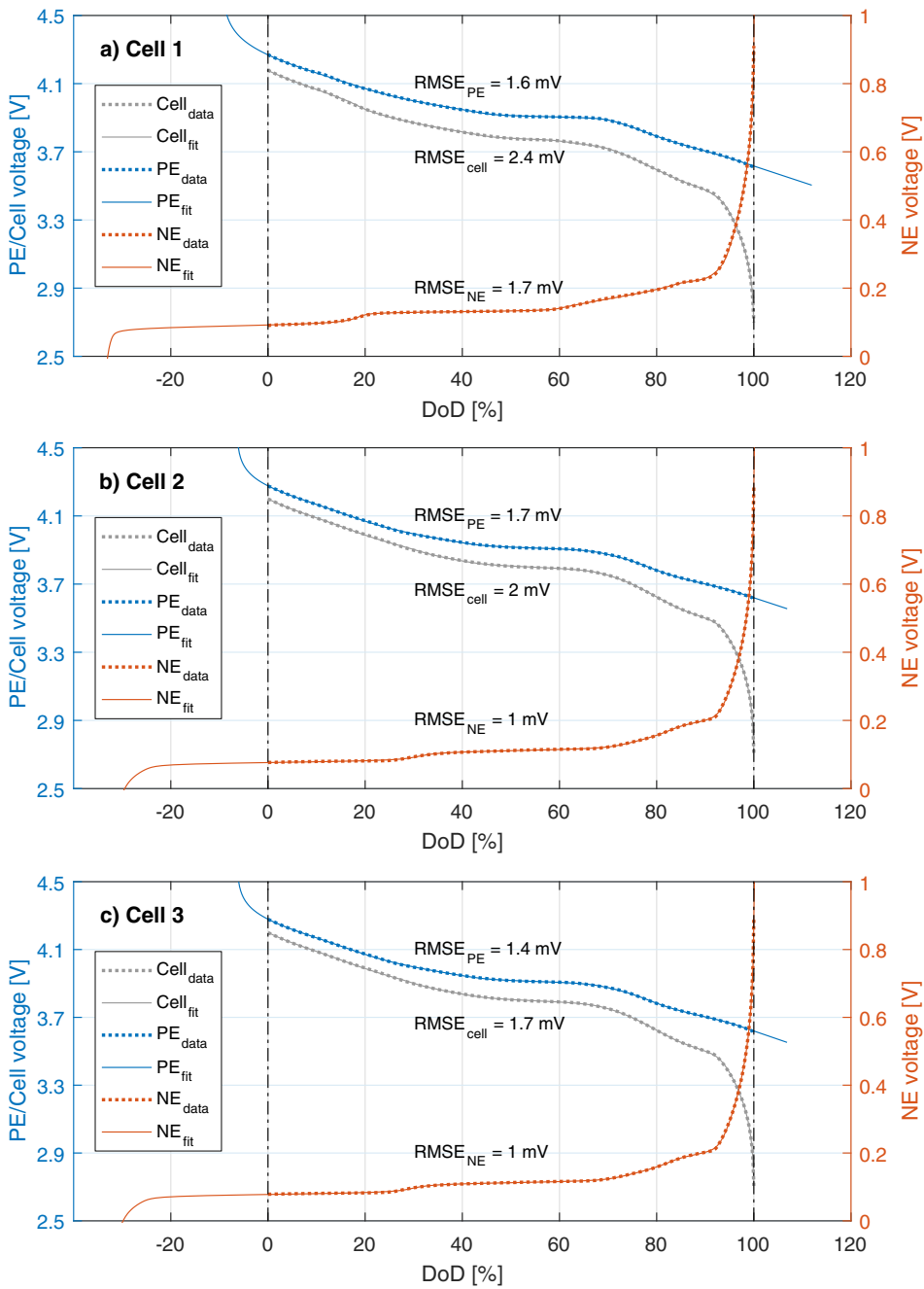


Figure 2. Pseudo-OCV measurements and fit results of 3-electrode cells a) cell 1, b) cell 2 and c) cell 3.

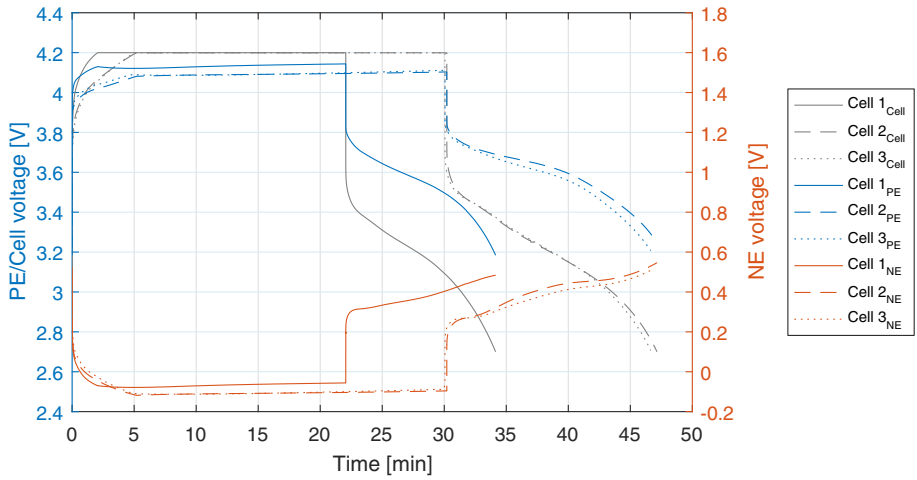


Figure 3. Voltage of 3-electrode cells during 2 C cycle at -10°C.

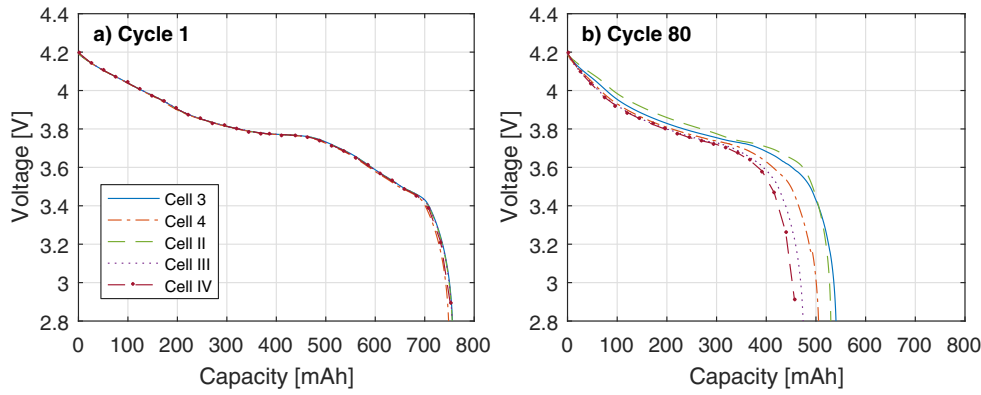


Figure 4. Pseudo-OCV measurements of 3-electrode cells and unmodified cells a) at cycle 1 and b) at cycle 80.

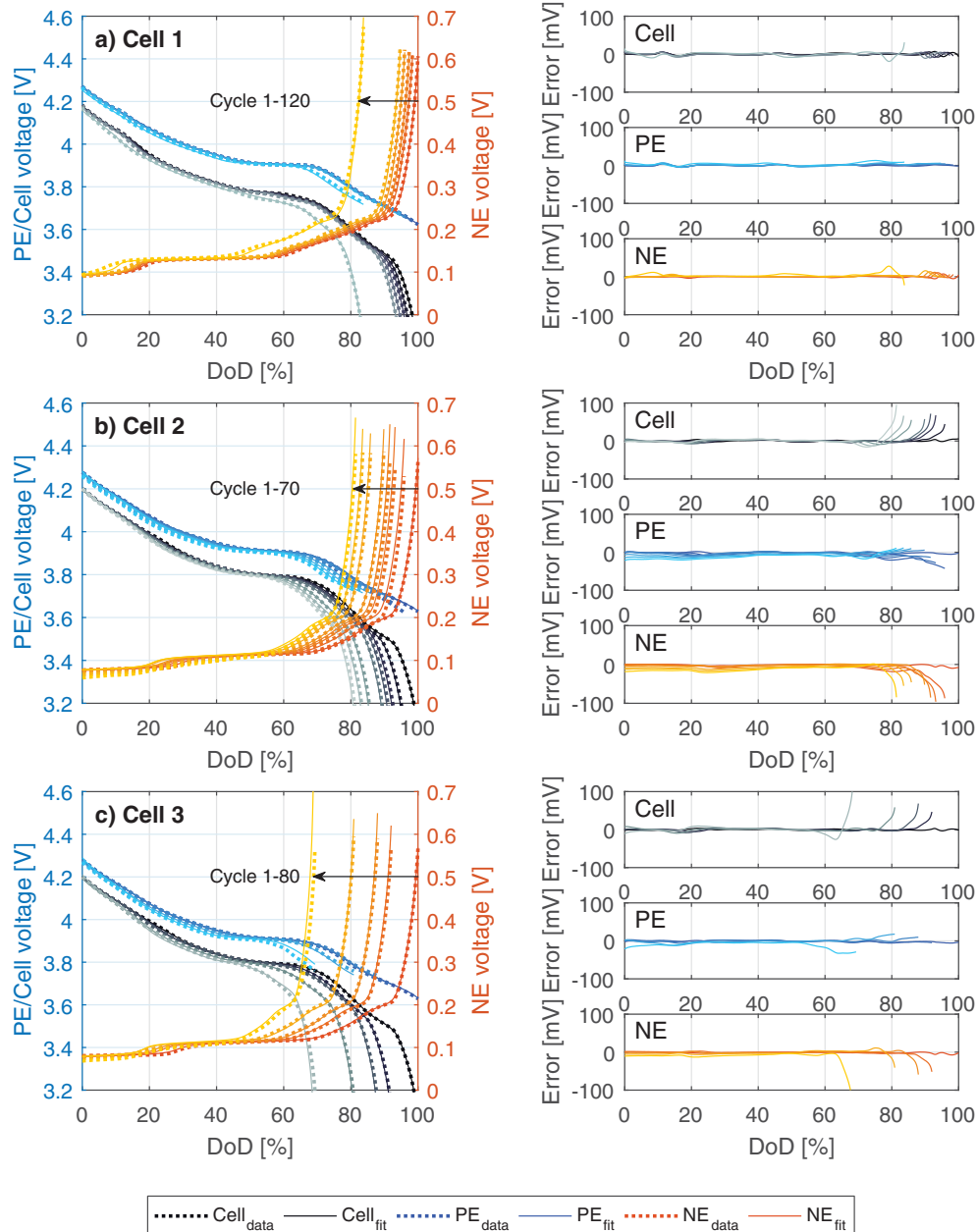


Figure 5. Pseudo-OCV fitting results a) cell 1, b) cell 2 and c) cell 3.

Table V. Maximal RMSE values of all characterization cycles.

	Cell [mV]	PE [mV]	NE [mV]
Cell 1	5	5	7
Cell 2	7	13	14
Cell 3	10	13	16

LAM_{PE} and LAM_{NE} depend on the qualities of pseudo-OCV fits of the PE and NE, respectively. LLI depends on the fitting quality of both PE and NE. Error bars for the estimated LAM_{PE} and LAM_{NE} are derived from the RMSE on the estimated, normalized capacity of the PE and NE, respectively. Error bars for the estimated LLI are based on the sum of the RMSE on the estimated, normalized capacity of PE and NE. The RMSE on estimated capacity is calculated by

$$\text{RMSE}_x = \sqrt{\frac{\sum_{i=1}^n (x_i(E_i^{\text{OC}}) - \hat{x}_i(\hat{E}_i^{\text{OC}}))^2}{n}} \cdot 100\% \quad [19]$$

for each the PE and the NE capacity, where $x_i(E_i^{\text{OC}})$ is the measured, normalized capacity, $\hat{x}_i(\hat{E}_i^{\text{OC}})$ is the fitted, normalized capacity and n is the number of measurements.

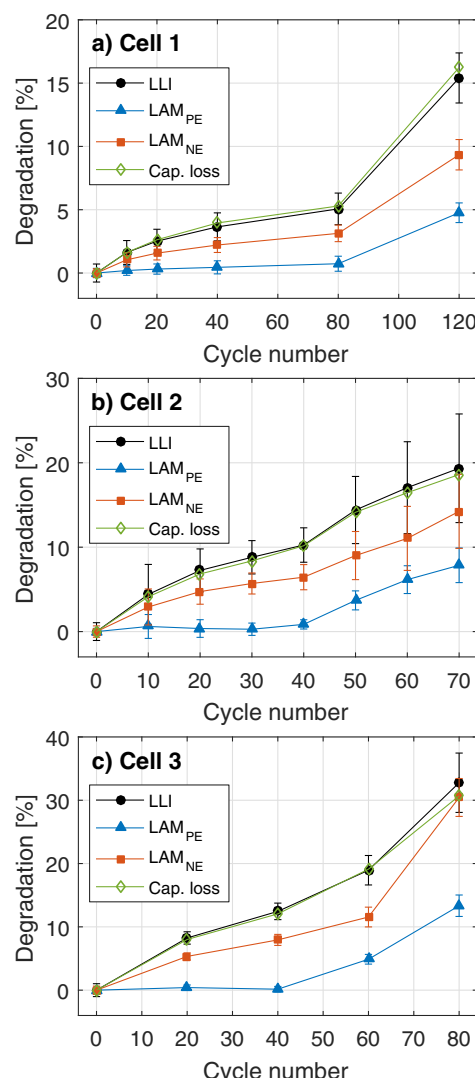


Figure 6. Capacity loss and estimated degradation modes of a) cell 1, b) cell 2 and c) cell 3.

High fitting accuracies were achieved for PE voltages of all cells with uncertainties on LAM_{PE} (expressed by error bars) not exceeding $\pm 2\%$. Uncertainties on LAM_{NE} are higher at up to $\pm 4\%$ and, consequently, uncertainties on LLI are up to $\pm 6\%$. Uncertainties of estimated degradation modes are generally highest for cell 2.

The evolution of degradation modes over the cells' life shows that cycling at -10°C primarily affects the NE, as reflected by a rapid rise in LAM_{NE}. The extended CV charging periods at -10°C , experienced by cells 2 and 3, caused greater rates of degradation than exhibited by cell 1. By cycle 80, cell 1 had lost roughly 5% of capacity and 3-4% of active NE material. By comparison, cell 3 had lost 30% of capacity by cycle 80 and the same amount of active NE material. By the end of tests (cycle 120), cell 1 sustained $\sim 5\%$ LAM_{PE} and $\sim 10\%$ of LAM_{NE}. Cells 2 and 3 had lost close to 10% of active PE material, as well as $\sim 15\%$ and $\sim 30\%$ of LAM_{NE}, respectively, by the end of tests (cycle 70). Cells 2 and 3 showed very similar modes of degradation up until cycle 60. The onset of LAM_{PE} did not occur before cycle 40 for both cells. The higher frequency of characterization cycles recorded on cell 2 did not cause major differences in degradation compared to cell 3 for most of the cells' cycle life.

This analysis shows that the presented diagnostic algorithm can be used to accurately detect LAM_{NE}, LAM_{PE} and LLI, as confirmed by the OCV measurements recorded on the 3-electrode cells. Cycling the cells at -10°C and 2 C was expected to primarily affect the NE due to the deposition and subsequent partial stripping of lithium on the graphite particles, which is likely to occur under these conditions.⁷ Negative NE potentials and metallic lithium deposits on graphite particles may have caused the formation of surface films, which block active NE sites, resulting in an effective loss of active NE material. High rates of LAM_{NE} in turn increase the likelihood of further lithium plating, which could be detected using the presented method.

SEM and EDX results.—Post-mortem analyses by means of SEM and EDX were conducted in order to provide further experimental validation of the degradation modes estimated in Estimation of degradation modes section. SEM images were recorded on NE and PE samples of the pristine cell 0, which had not been cycled (Figures 7a and 7b), of cell 4 after 80 cycles (Figures 7c and 7d) and of cell II after 80 cycles (Figures 7e and 7f). Comparing the images in Figure 7 allows for a qualitative comparison of the morphology of the NE surface (left column) and the PE surface (right column). The most significant differences can be observed between the NE surface of the pristine cell and the cycled cells. While the graphite surface of the pristine cell in Figure 7a appears largely smooth, the surfaces of the cycled cells in Figures 7c and 7e are covered in mossy deposits. EDX analyses were conducted in order to reveal the composition of these deposits. There is no discernible difference between the NE surfaces of the 3-electrode cell 4 and the unmodified cell II.

In contrast to the NE, no significant differences can be observed between the PE surfaces of the pristine and the cycled cells (Figures 7b, 7d and 7f). These findings are in line with the estimated degradation modes; the NEs were expected to be more heavily affected by the low-temperature cycling procedures than the PEs.

EDX spectra were recorded on NE and PE samples of the pristine cell 0, the 3-electrode cell 1 and the unmodified cell I after 120 cycles, and on samples of the 3-electrode cell 4 and the unmodified cell II after 80 cycles. Figure 8 shows the color-coded, layered images of NE samples (left column) and PE samples (right column) of the pristine cell 0 (Figures 8a and 8b), the 3-electrode cell 4 (Figures 8c and 8d) and the unmodified cell II (Figures 8e and 8f).

The EDX color map of the pristine NE sample of cell 0 in Figure 8a shows a surface mainly consisting of pure carbon, illustrated in red. It should be pointed out that the pristine cell was purchased as a commercial product, which would have undergone the typical SEI formation procedure, consisting of a number of formation cycles. The SEI is most likely too thin to be detected by EDX. The NE surfaces of cell 4 and cell II in Figures 8c and 8e appear to be partially coated with oxygen-rich deposits, illustrated in cyan. The surface film on the NEs appears to be discontinuous – some uncoated graphite is still visible,

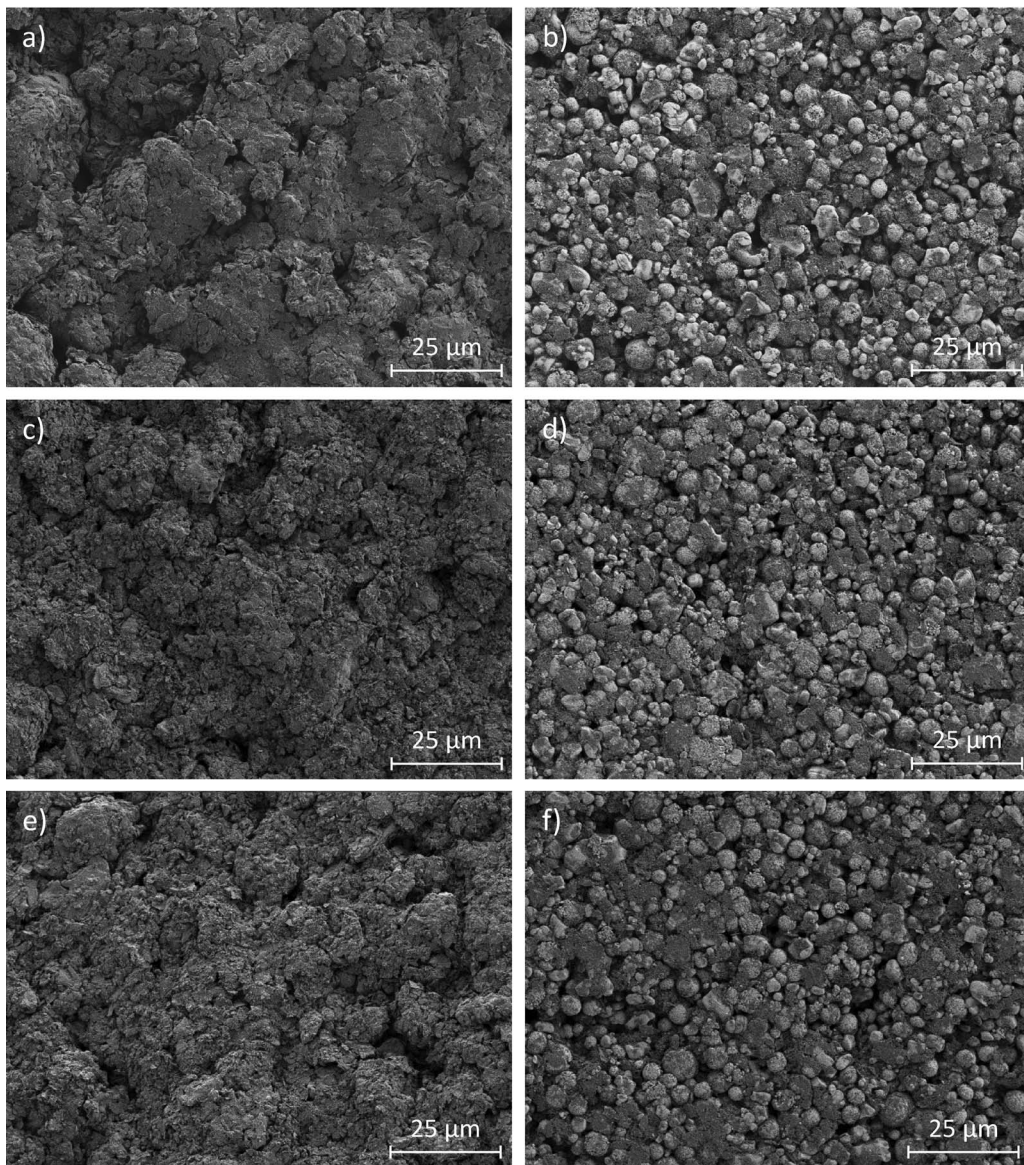


Figure 7. SEM images of NE (left column) and PE (right column) of pristine cell 0 (a, b), cell 4 after 80 cycles (c, d) and cell II after 80 cycles (e, f). Surface films on the cycled NEs appear as mossy deposits in c) and e).

illustrated in red in Figures 8c and 8e, whereas the surface film has a yellow/orange color. The thickness of the surface film could not be measured with the applied methods. Measuring the thickness would require a study of the cross section of the NE electrodes.

The weight percentages of the elements detected on the NE samples of the pristine and cycled cells are listed in Table VI. The quantitative results for the pristine NE reveal that no oxygen was detected. In case of the cycled cells, however, significant amounts of oxygen, on the order of 25 wt%, were found on all cycled NE. Moreover, the fraction of fluorine decreased from roughly 11% detected on the pristine NE, to 5–7% on the cycled NEs. Fluorine forms part of the electrolyte in most commercial cells. It is well documented in the literature that electrolyte solvents and additives are reduced at the graphite surface to form carbonates.^{29,30} In this study the NE potential of the test subjects was frequently pushed below zero, which likely led to deposition of metallic lithium on the graphite surface. No microscopical evidence of metallic lithium on the graphite surface could be observed because lithium is too light to be detected with standard SEM or EDX methods. Negative NE potentials may also have accelerated the rate of solvent and/or additive reduction at the NE, which may have contributed to

the formation of surface films. Another possible origin of the surface films could be from metallic lithium irreversibly deposited on the NEs during low-temperature charging. The transfer of the NE samples in air may have subsequently oxidized the metallic lithium, contributing to the surface films observed on the NEs. The surface deposits observed on the NE of the cycled cells are unlikely to be typical SEI, since a SEI was already present on the pristine cell and could not be detected by EDX. Similar weight percentages of carbon and oxygen found on the NEs of the 3-electrode cells and of the unmodified cells suggest that the NE of both cells experienced the same mode of degradation.

The EDX color maps of the PEs sample of cell 0 (pristine), cell 4 and cell II are shown in Figures 8b, 8d and 8f, respectively. Unlike in the case of the NEs, there are no obvious differences in the EDX color maps between the PE sample of the pristine cell and the samples of the cycled cells.

The quantitative results, listed in terms of wt% in Table VII, do not show any significant differences in PE composition either. The results obtained from the diagnostic algorithm indicate small amounts of LAM_{PE}. These losses of active material could be due to particle cracking resulting from thermal cycling. However, no cracks in the

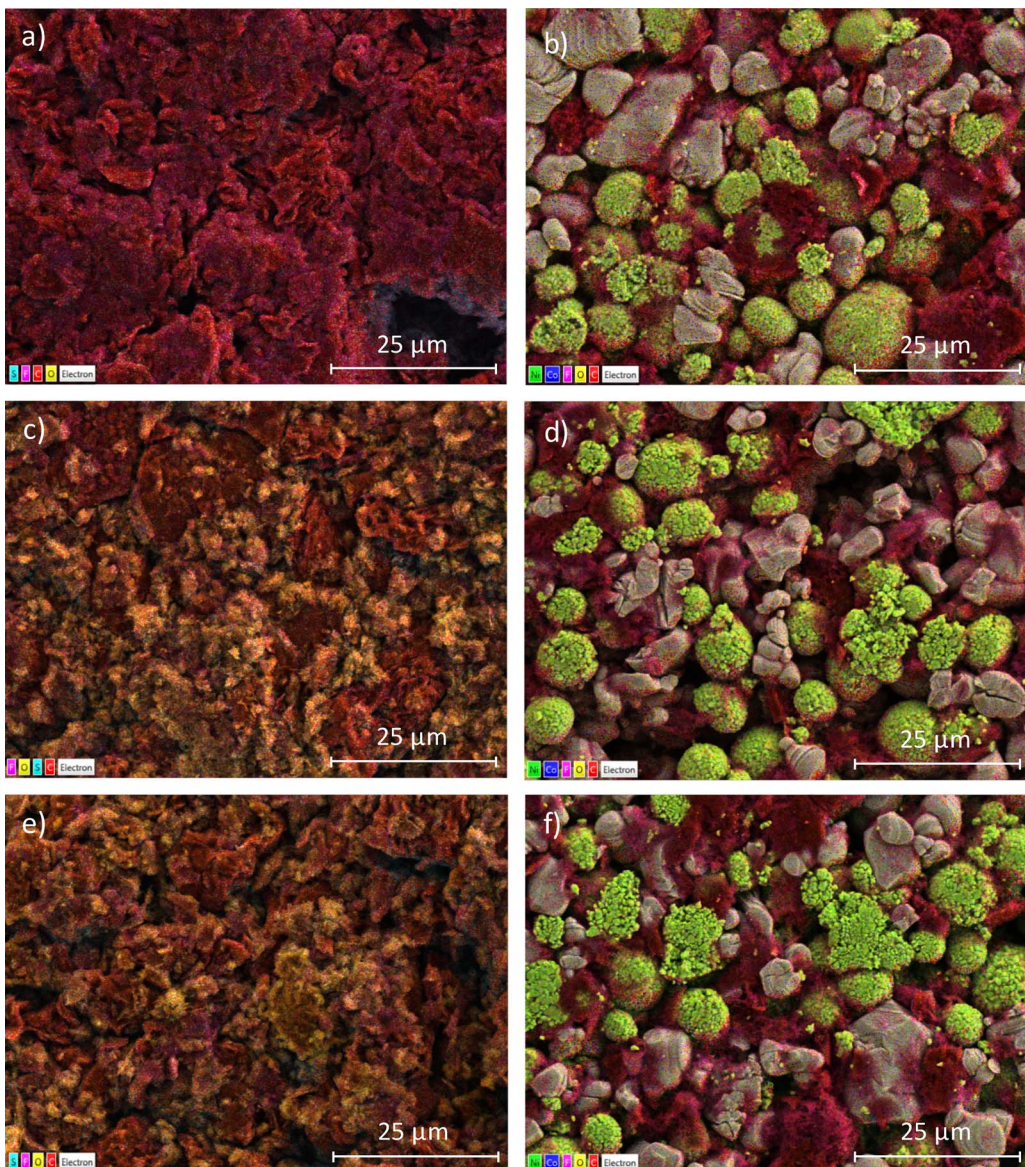


Figure 8. Layered EDX images of NE (left column) and PE (right column); a), b) cell 0 (pristine), c), d) cell 4 and e), f) cell II. Surface films on the cycled NEs appear in orange/yellow in c) and e).

electrode material were observed by way of the presented SEM analysis, which indicates that such cracks would either be too small to be observed in the recorded micrographs or the cracks may have occurred between particles, which would be difficult to identify by an optical analysis of SEM micrographs. Another possible reason for LAM_{PE} could be electrical contact loss between particles of active material, active material and carbon particles or between active material and current collector. Contact loss between the active material and the current collector would require the study of the cross section of the electrode sheets, which was not possible in this work. The formation

of surface films, too thin to detect with EDX, could also account for LAM_{PE}. Surface films on LCO and NCO materials can reportedly consist of carbonates as well as polymers and polycarbonates³¹ and may block active sites on the PE material.

Overall, the SEM and EDX results revealed a clear change in surface morphology and composition of the NEs of the cycled cells. These findings support the results obtained from the diagnostic algorithm, which identified LAM_{NE} as the primary source of degradation in the low-temperature tests. No physical reason for the loss of active PE

Table VI. Weight % of carbon, oxygen, fluorine and sulfur in NEs.

Cell ID	C	O	F	S
Cell 0	88.3%	0.0%	10.9%	0.5%
Cell 1	67.5%	25.8%	5.2%	1.1%
Cell I	68.2%	25.3%	4.9%	1.1%
Cell 4	65.0%	26.6%	6.7%	1.2%
Cell II	66.8%	24.9%	7.0%	0.8%

Table VII. Weight % of cobalt, nickel, carbon, oxygen and fluorine in PEs.

Cell ID	Co	Ni	C	O	F
Cell 0	19.4%	11.4%	41.0%	20.4%	6.9%
Cell 1	23.1%	10.6%	38.3%	21.1%	6.2%
Cell I	21.4%	15.3%	37.0%	21.0%	4.6%
Cell 4	23.5%	16.4%	33.1%	21.0%	5.3%
Cell II	19.0%	13.5%	40.1%	20.4%	6.9%

material was found using SEM and EDX. There was no discernible difference in degradation between the 3-electrode cells and the unmodified cells, suggesting that the modification does not affect the cells' performance and cycle life.

Conclusions

3-electrode cells and unmodified cells were exposed to extreme cycling conditions with charge and discharge rates of 2 C and an ambient temperature of -10°C . The harsh conditions pushed the NE potential below 0 V for every charging step. This favored lithium plating on the graphite NEs and rapid rates of NE degradation were expected. The diagnostic algorithm introduced in Ref. 26 was applied to estimate the degradation modes in the tested cells by fitting the cells' measured pseudo-OCVs.

The use of the 3-electrode cells allowed, for the first time, to validate degradation diagnostics on commercial pouch cells by comparing the modeled and measured electrode voltages. Small differences between the modeled and measured electrode voltages indicate that the diagnostic algorithm accurately captures the effects of degradation in the tested cells. LAM_{NE} was identified as the predominant degradation mode, which was expected, given that the NE was frequently driven to negative voltages, increasing the likelihood of metallic lithium deposition and increased surface film formation. SEM and EDX results support this finding by revealing oxygen-rich deposits on the NEs of the cycled cells.

The comparison of electrical test results and post-mortem results of the 3-electrode cells and the unmodified cells demonstrate that the insertion of the reference electrode into the pouch cells did not noticeably alter the degradation of the modified cells.

The findings presented in this work confirm that it is possible to identify potential safety hazards, in the form of rapid and excessive NE degradation, using the proposed diagnostic algorithm.

Acknowledgments

This work was funded by the EPSRC and Jaguar Land Rover.

References

- Bloom, B. Cole, J. Sohn, S. Jones, E. Polzin, V. Battaglia, G. Henriksen, C. Motloch, R. Richardson, T. Unkelhaeuser, D. Ingwersen, and H. Case, An accelerated calendar and cycle life study of Li-ion cells, *Journal of Power Sources*, **101**(2), 238 (2001).
- S. S. Choi and H. S. Lim, Factors that affect cycle-life and possible degradation mechanisms of a Li-ion cell based on LiCoO_2 , *Journal of Power Sources*, **111**, 130 (2002).
- J. Vetter, P. Novák, M. Wagner, C. Veit, K.-C. Möller, J. Besenhard, M. Winter, M. Wohlfahrt-Mehrens, C. Vogler, and A. Hammouche, Ageing mechanisms in lithium-ion batteries, *Journal of Power Sources*, **147**(1-2), 269 (2005).
- P. Arora, M. Doyle, and R. E. White, Mathematical Modeling of the Lithium Deposition Overcharge Reaction in Lithium-Ion Batteries Using Carbon-Based Negative Electrodes, *Journal of The Electrochemical Society*, **146**(10), 3533 (1999).
- C. Monroe and J. Newman, Dendrite Growth in Lithium/Polymer Systems, *Journal of The Electrochemical Society*, **150**(10), A1377 (2003).
- S. Santhanagopalan, P. Ramadas, and J. Z. Zhang, Analysis of internal short-circuit in a lithium ion cell, *Journal of Power Sources*, **194**(1), 550 (2009).
- M. Petzl and M. A. Danzer, Nondestructive detection, characterization, and quantification of lithium plating in commercial lithium-ion batteries, *Journal of Power Sources*, **254**, 80 (2014).
- S. U. Kim, P. Albertus, D. Cook, C. W. Monroe, and J. Christensen, Thermoelectrochemical simulations of performance and abuse in 50-Ah automotive cells, *Journal of Power Sources*, **268** (2014) 625.
- S. Tippmann, D. Walper, L. Balboa, B. Spier, and W. Bessler, Low-Temperature Charging of Lithium-ion Cells Part I: Electrochemical Modeling and Experimental Investigation of Degradation Behavior, *Journal of Power Sources*, **252**, 305 (2014).
- J. Remmlinger, S. Tippmann, M. Buchholz, and K. Dietmayer, Low-temperature charging of lithium-ion cells Part II: Model reduction and application, *Journal of Power Sources*, **254**, 268 (2014).
- T. Waldmann, M. Wilka, M. Kasper, M. Fleischhammer, and M. Wohlfahrt-Mehrens, Temperature dependent aging mechanisms in Lithium-ion batteries – A Post-Mortem stud, *Journal of Power Sources*, **262**, 129 (2014).
- M. Petzl, M. Kasper, and M. A. Danzer, Lithium plating in a commercial lithium-ion battery – A low-temperature aging study, *Journal of Power Sources*, **275**, 799 (2015).
- K. Jalkanen, J. Karppinen, L. Skogström, T. Laurila, M. Nisula, and K. Vuorilehto, Cycle aging of commercial NMC/graphite pouch cells at different temperatures, *Applied Energy*, **154**, 160 (2015).
- A. Marongiu, N. Nlandi, Y. Rong, and D. U. Sauer, On-board capacity estimation of lithium iron phosphate batteries by means of half-cell curves, *Journal of Power Sources*, **324**, 158 (2016).
- J. Jaguemont, L. Boulon, P. Venet, Y. Dubé, and A. Sari, Lithium-Ion Battery Aging Experiments at Subzero Temperatures and Model Development for Capacity Fade Estimation, *IEEE Transactions on Vehicular Technology*, **65**, 4328 (2016).
- D. Anseán, M. Dubarry, A. Devie, B. Y. Liaw, V. M. García, J. C. Viera, and M. González, Operando lithium plating quantification and early detection of a commercial LiFePO_4 cell cycled under dynamic driving schedule, *Journal of Power Sources*, **356**, 36 (2017).
- L. E. Downie, L. J. Krause, J. C. Burns, L. D. Jensen, V. L. Chevrier, and J. R. Dahn, In-Situ Detection of Lithium Plating on Graphite Electrodes by Electrochemical Calorimetry, *Journal of The Electrochemical Society*, **160**(4), 588 (2013).
- S. Alavi, M. Samadi, and M. Saif, Plating Mechanism Detection in Lithium-ion batteries, by using a particle-filtering based estimation technique, *American Control Conference*, 4356 (2013).
- B. Bitzer and A. Gruhle, A new method for detecting lithium plating by measuring the cell thickness, *Journal of Power Sources*, **262**, 297 (2014).
- C. Birkenmaier, B. Bitzer, M. Harzheim, A. Hintennach, and T. Schleid, Lithium Plating on Graphite Negative Electrodes: Innovative Qualitative and Quantitative Investigation Methods, *Journal of The Electrochemical Society*, **162**(14), A2646 (2015).
- C. Uhlmann, J. Illig, M. Ender, R. Schuster, and E. Ivers-Tiffée, In situ detection of lithium metal plating on graphite in experimental cells, *Journal of Power Sources*, **279**, 428 (2015).
- J. C. Burns, D. A. Stevens, and J. R. Dahn, In-Situ Detection of Lithium Plating Using High Precision Coulometry, *Journal of The Electrochemical Society*, **162**(6), A959 (2015).
- S. Schindler, M. Bauer, M. Petzl, and M. A. Danzer, Voltage relaxation and impedance spectroscopy as in-operando methods for the detection of lithium plating on graphitic anodes in commercial lithium-ion cells, *Journal of Power Sources*, **304**, 170 (2016).
- S. S. Zhang, K. Xu, and T. R. Jow, Study of the charging process of a LiCoO_2 -based Li-ion battery, *Journal of Power Sources*, **160**, 1349 (2006).
- S. Tippmann, D. Walper, L. Balboa, B. Spier, and W. G. Bessler, Low-Temperature Charging of Lithium-ion Cells Part I: Electrochemical Modeling and Experimental Investigation of Degradation Behavior, *Journal of Power Sources*, **252**, 305 (2013).
- C. R. Birk, M. R. Roberts, E. McTurk, P. G. Bruce, and D. A. Howey, Degradation Diagnostics for Lithium Ion Cells, *Journal of Power Sources*, **341**, 373 (2017).
- C. R. Birk, E. McTurk, M. R. Roberts, P. G. Bruce, and D. A. Howey, A Parametric Open Circuit Voltage Model for Lithium Ion Batteries, *Journal of The Electrochemical Society*, **162**(12), A2271 (2015).
- E. McTurk, C. R. Birk, M. R. Roberts, D. A. Howey, and P. G. Bruce, Minimally Invasive Insertion of Reference Electrodes into Commercial Lithium-Ion Pouch Cells, *ECS Electrochemistry Letters*, **4**(12), A145 (2015).
- D. Aurbach, B. Markovsky, I. Weissman, E. Levi, and Y. Ein-Eli, On the correlation between surface chemistry and performance of graphite negative electrodes for Li ion batteries, *Electrochimica Acta*, **45**(1-2), 67 (1999).
- Y. Wang, S. Nakamura, M. Ue, and P. B. Balbuena, Studies To Understand Surface Chemistry on Carbon Anodes for Lithium-Ion Batteries: Theoretical Reduction Mechanisms of Ethylene Carbonate, *Journal of the American Chemical Society*, **123**(47), 11708 (2001).
- K. Edström, T. Gustafsson, and J. Thomas, The cathodeelectrolyte interface in the Li-ion battery, *Electrochimica Acta*, **50**(2-3), 397 (2004).